Time-Domain Propagation Measurements of the NASA Space-Power Facility

Robert T. Johnk
John D. Ewan
Paul M. McKenna
Ronald L. Carey
Nicholas DeMinco

report series

U.S. DEPARTMENT OF COMMERCE · National Telecommunications and Information Administration

Time-Domain Propagation Measurements of the NASA Space-Power Facility

Robert T. Johnk
John D. Ewan
Paul M. McKenna
Ronald L. Carey
Nicholas DeMinco

U.S. DEPARTMENT OF COMMERCE

September 2010

DISCLAIMER

Certain commercial equipment and materials are identified in this report to specify adequately the technical aspects of the reported results. In no case does such identification imply recommendations or endorsement by the National Telecommunications and Information Administration, nor does it imply that the material or equipment identified is the best available for this purpose.

CONTENTS

FIGURES

ABBREVIATIONS/ACRONYMS

dB   decibel

DOC   Department of Commerce

E3   Electromagnetic Environmental Effects

FDTD   Finite Difference Time Domain

ITS   Institute for Telecommunication Sciences

LPDA   Log-Periodic Dipole Array

NASA   National Aeronautics and Space Administration

NIST   National Institute of Standards and Technology

NTIA   National Telecommunications and Information Administration

RF   Radio Frequency

SPF   NASA Space Power Facility located in Sandusky, Ohio

TIME-DOMAIN PROPAGATION MEASUREMENTS OF THE NASA SPACE-POWER FACILITY

Robert T. Johnk, John D. Ewan, Paul M. McKenna, Ronald L. Carey, Nicholas DeMinco[1]

This report describes a recent measurement effort conducted by the Institute for Telecommunication Sciences at a chamber located at the NASA Space Power Facility (SPF) in Sandusky, Ohio. The report describes the chamber and the measurement system, and provides some selected time- and frequency-domain results. A detailed description of the measurement procedures and post-processing is provided. The results obtained indicate that the SPF chamber exhibits robust reverberant behavior. The flexibility and efficiency of time-domain measurements is also demonstrated.

Keywords: antenna; biconical; chamber; decay time; direct pulse; discone; electromagnetic; finite-difference time-domain; fast Fourier transform; impulse; joint time-frequency analysis; log-periodic; oscilloscope; reverberation; ultra wideband.

1 INTRODUCTION

This report describes a recent measurement effort [1] conducted by a team of engineers from the Institute for Telecommunication Sciences (NTIA/ITS) at the Space Power Facility (SPF), located at the NASA Plumbrook station in Sandusky, Ohio. The SPF houses the world's largest space environment simulation chamber, and is used to test various types of space hardware. In addition, we present the results of a simulation using a rotationally-symmetric, finite-difference time-domain (FDTD) model of the SPF.

The measurement campaign was carried out using a direct-pulse time-domain transmission system. The system measures the time-domain response of the chamber to a short-duration pulse that is transmitted and received by a pair of broadband antennas. In this series of tests, three sets of antennas were used to perform transmission measurements, covering the frequency range of 20–1500 MHz. The digitized impulse-response data were post-processed to obtain chamber parameters like insertion loss and decay time, which are useful to assess suitability of the SPF for electromagnetic environmental effects (E3) testing. This effort was intended to provide baseline data for Finite-Difference Time-Domain (FDTD) numerical models of the SPF that were under development at ITS. The full-bandwidth data obtained from these measurements were also intended to provide a basis for accurate and representative numerical simulations.

The measurements indicate that the chamber exhibits robust reverberant behavior with excellent statistical field uniformity throughout the proposed test volume. In addition, the chamber exhibits decay rates that are a function of frequency and vary over the range of 15-50 μsec. These long decay times result from a combination of large chamber volume and high-conductivity aluminum walls.

---

[1] The authors are with the Institute for Telecommunication Sciences, National Telecommunications and Information Administration, U.S. Department of Commerce, Boulder, CO 80305.

2   DESCRIPTION OF THE NASA SPACE-POWER FACILITY

NASA is proposing to perform future E3 testing within the SPF vacuum chamber, which is an all-aluminum, hemisphere-on-cylinder vessel 100 feet (30.5 m) in diameter and 122 feet (37.2 m) high. The E3 testing will be performed at normal atmospheric pressure and temperature, with the test article positioned upright near the center of the chamber floor. Figure 1 shows a test article being configured for tests inside the chamber. Radio-frequency test equipment will be used around the periphery of a space vehicle to conduct system-level radiated susceptibility testing. The unique shape, large volume, and high inner-surface reflectivity of the SPF vacuum chamber will create a complex electromagnetic field structure inside the chamber. To minimize risk to the vehicle under test, it is necessary to thoroughly understand the electromagnetic propagation and reverberation characteristics within the chamber volume of the SPF. NASA wants to create known electric-field strengths throughout the vacuum chamber, and minimize regions of localized high-level radio-frequency electromagnetic field levels. NASA also needs to design measurement systems that function optimally within this unique environment.

Figure 1. The SPF vacuum chamber with typical test article. Note the large access doors and buttresses in front of and behind the rocket.

3 TIME-DOMAIN MEASUREMENT SYSTEM

The time-domain measurement system is shown in Figure 2. It consists of an impulse generator, a 12 GHz bandwidth high-speed oscilloscope, two broadband antennas, a trigger generator, and precision microwave coaxial cables. This system is similar to one used in an earlier chamber evaluation effort [2]. The trigger generator, located outside of the chamber, produces a 1 kHz square wave that activates the impulse generator and, at the same instant, initiates an oscilloscope sweep. The impulse generator generates a repetitive sequence of 35 V (peak) impulses, each with a base width of approximately 1 ns.

The system is first calibrated by providing a direct connection between the transmitting and receiving antenna cables (Fig. 2(a)). The generator waveform is attenuated, digitized, and stored for subsequent analysis. This step is needed to provide a reference signal to determine chamber insertion loss. A 35-dB attenuator is used to provide proper signal conditioning for the oscilloscope to prevent distortion or damage to the oscilloscope circuitry. Next, the cables are hooked to the transmitting and receiving antennas, and transmission measurements are performed within the chamber environment. The impulse generator transmits a series of unipolar pulses at a repetition rate of 1 kHz. The transmitted pulses undergo multiple reflections from the chamber boundaries, and are received by the oscilloscope then digitized. The system is operated in a repetitive mode, and 200 averages are performed on the received waveforms to achieve an improvement of more than 20 dB in signal-to-noise ratio. Three sets of commercially-available transmitting and receiving antennas, with different frequency ranges, were used for the SPF evaluation: 1) biconical (20–300 MHz), 2) discone (100–1300 MHz), and 3) log-periodic (300–7000 MHz).
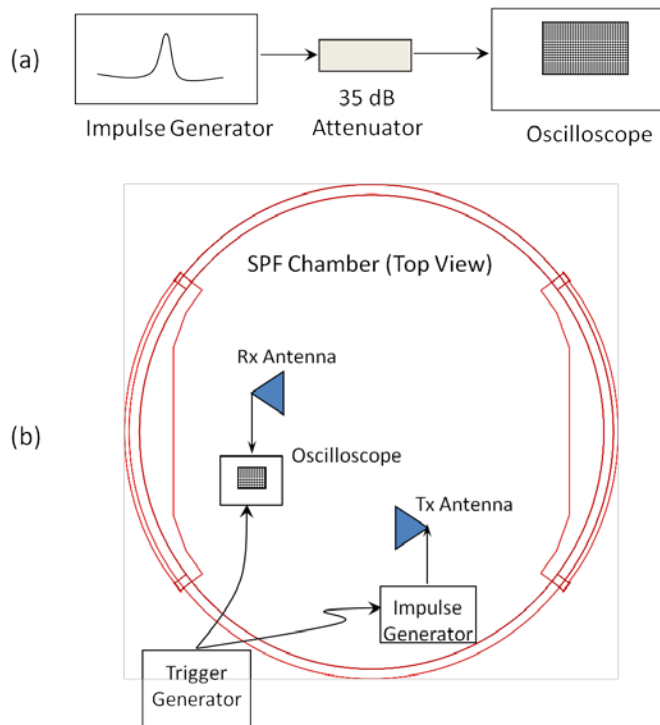
Figure 2. Measurement system setups. (a) Calibration. (b) Chamber transmission measurement. A trigger generator was used for only the horizontal scans.

4   MEASUREMENT SEQUENCES

Measurement sequences were performed at the locations shown in Figures 3(a) and (b). Horizontal scans were carried out with the transmitting antennas mounted on dielectric masts and carts shown in Figure 4. Each scan was repeated with the three types of antennas. The transmitting cart remained at a fixed location for the first two horizontal scans. The transmitting antenna cart was parked at the center position for scan 1 with the antenna set at a height of 22' (6.7 m). The receiving cart was moved to positions 1–10, shown in Figure 3(b). The receiving antenna was set at a height of 22' (6.7 m) for positions 1–10. Data were also taken with a lower receiving antenna height of 10' at positions 2,3,7,9 for the biconical antennas only. The transmitting antenna was also vertically polarized throughout the horizontal scans. Data were taken with the receiving antenna vertically (vpol) and then horizontally polarized (hpol) at the 22' (6.7 m) height. The receiving antenna was vertically polarized for all of the 10' (3.05 m) measurements. A second horizontal scan was performed with the transmitting antenna cart parked at position 7. Data were acquired for all antenna types with the receiver at positions 1–6 and the antennas vertically polarized at 22' (6.7 m). A limited set was taken at the 10' (3.05 m) height with the biconical antennas at the same positions.

A vertical scan was implemented by installing the pulse generator, a battery-powered UPS, and transmitting antenna on a plywood platform. The platform was supported by nylon rope to minimize spurious reflections. It was raised and lowered by personnel located just outside the top of the SPF chamber. The receiving antenna was parked at position 7 and measurements were performed with the transmitter parked at 10' (3.05 m) increments for heights of 50'–110' (15.2-33.5 m) above the chamber floor.
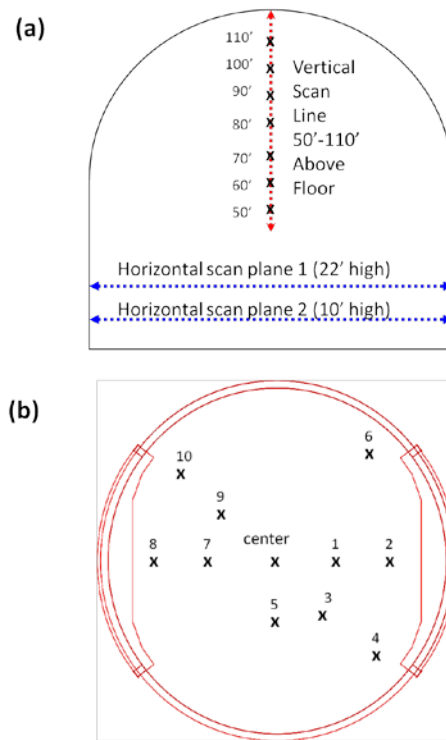
Figure 3. (a) Horizontal and vertical scan planes. (b) Antenna locations.
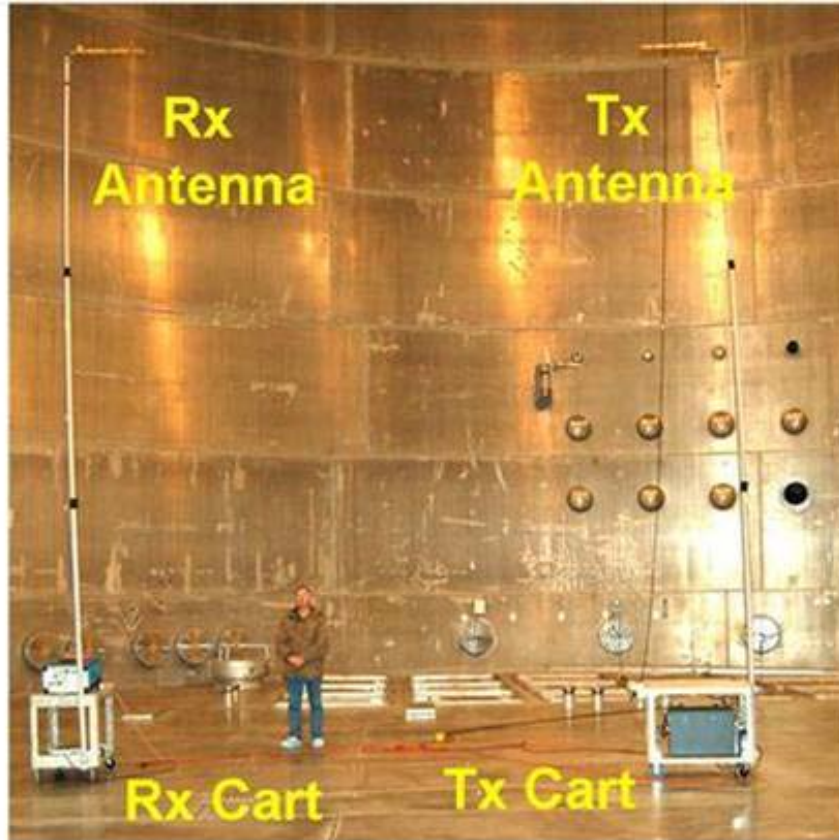
Figure 4. (a) Setup for horizontal scans. (b) Pulse generator inside a shielded box. (c) Oscilloscope mounted on receiving cart.

Figures 5 and 6 depict the vertical scan setup. A fixed transmitting orientation was maintained using nylon guy ropes at each scan position. The polarization of the receiving antenna was maintained in one configuration in the ascent portion of the scan and then switched during the

descent to achieve polarization diversity. A hard trigger connection was not used for the vertical scan because of the physical setup. Instead, the oscilloscope sweep was triggered internally at the onset of the received chamber signal.
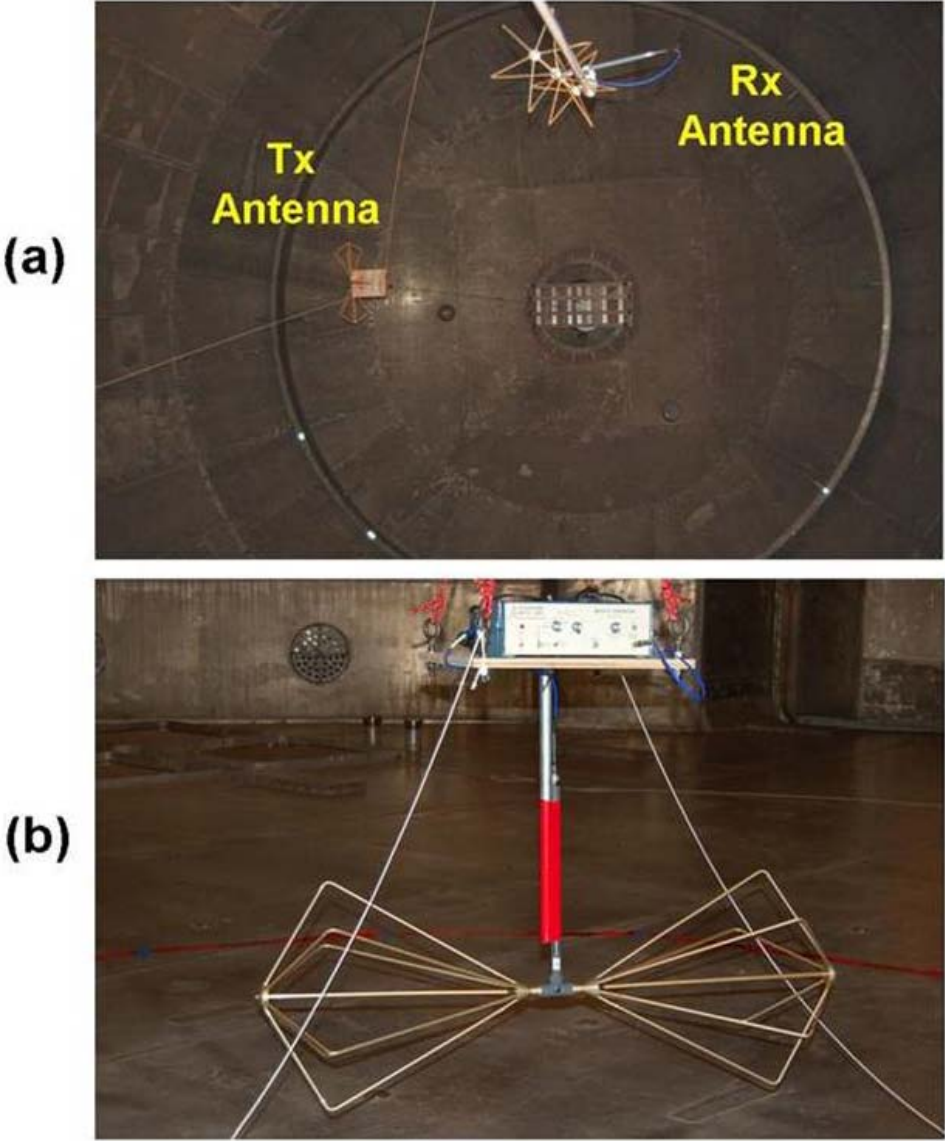
Figure 5. Test setup for the vertical scan. (a) System deployment. (b) Transmitter.

Figure 6. The vertical scan test setup with operator at the receiving cart. The transmitter is supported by nylon rope from above.

5   TIME-DOMAIN WAVEFORMS

Figure 7(a) depicts a reference waveform obtained from a conducted measurement with transmitting and receiving cables connected head-to-head through an attenuator. The resulting impulse has a width of approximately 1 ns, and has the amplitude spectrum shown in Figure 7(b). The useable frequency range for antenna-to-antenna measurements extends from the low-frequency limit of the antennas used, up to a maximum of approximately 1500 MHz. Figure 8 shows four oscilloscope waveforms obtained at positions 3 and 4 for two polarizations of the receiving discone antenna.

There are several striking aspects of these results. First, the temporal extent of the resulting waveforms is many tens of microseconds—a result of thousands of reflections from the chamber boundaries. The second salient feature is the single-exponential decay envelopes of the waveforms. An initial spike is noted for the vertically-polarized (vpol) case, which is caused by direct coupling between the antennas. In section 6, we will examine early-time behavior for the vertical scan, in which we observe focusing effects.

Perhaps the most interesting aspect is the similarity in waveform amplitudes for the four cases. This indicates that the chamber diffuses the propagating waves and provides a nearly equal split between the two polarizations. In fact, this trend was seen for all of the antenna types and scan positions. The result was unexpected. This diffusion might be caused by the large buttresses that support the access doors. More investigation will need to be conducted to understand the reasons for this.
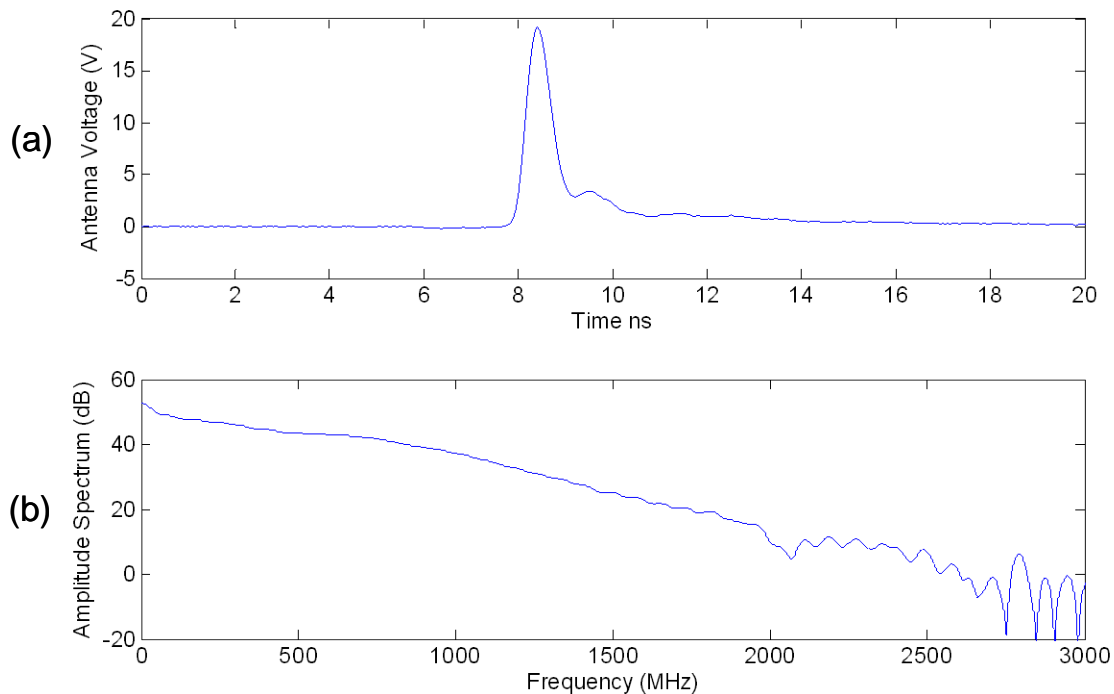
Figure 7. (a) Conducted generator waveform. (b) Conducted generator amplitude spectrum.
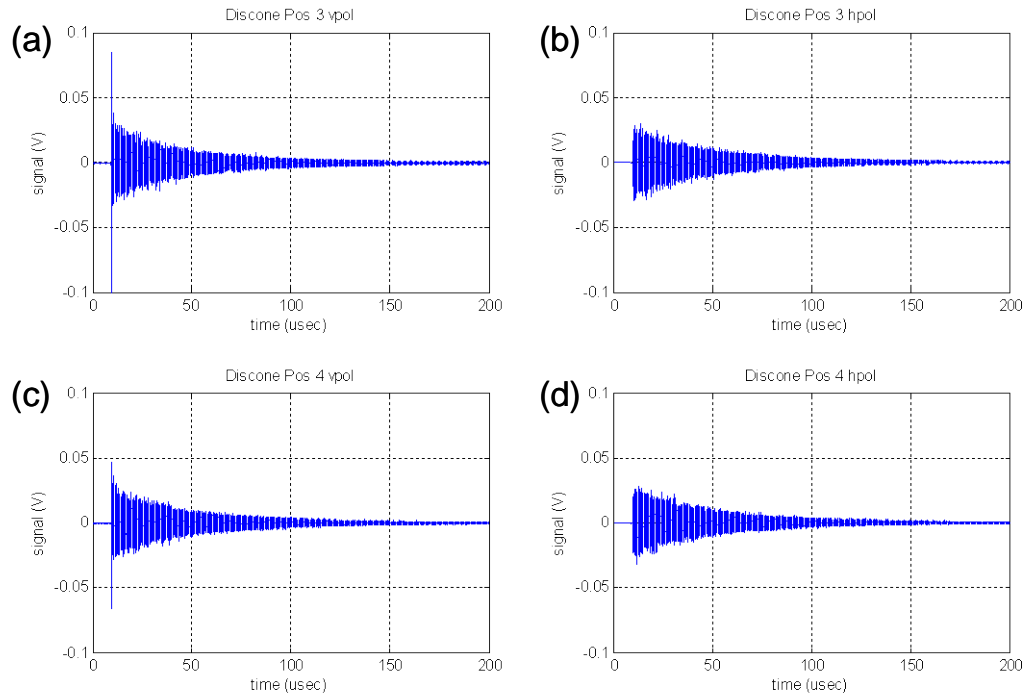
Figure 8. Received oscilloscope waveforms obtained with a discone antenna at (a) position 3, vpol. (b) position 3, hpol. (c) position 4, vpol. (d) position 4, hpol.

6   CHAMBER INSERTION GAIN

Insertion gain is computed from the chamber and reference waveforms. A fast Fourier transform is applied to each waveform and the frequency-domain results are normalized as shown in Figure 9(a). The result is the well-known transmission scattering parameter S_{21} with the reference planes located at the transmitting and receiving antenna connector ports. Converting the magnitude of S_{21} to dB obtains the insertion gain.

The transmission data are then electronically stirred [3],[4] by frequency averaging over a specified bandwidth, using the process depicted in Figure 9(b). The first step of the process consists of squaring the magnitude of the S_{21} results. This operation produces a scalar power at each FFT output bin, which can then be averaged over selected frequency ranges. The bins were averaged by entering a rectangular window on a selected FFT bin and averaging its power with those of adjacent bins. This is repeated by sliding the window to successive FFT bins and power averaging at each position.

An example of this is shown in Figure 9, where a 10 MHz wide sliding window is used. The measured time-domain waveform is shown in Figure 10(a), and it consists of an initial direct-coupling component, followed by an extended series of reflections from the chamber boundaries. The Fourier transform of this waveform is shown in Figure 10(b). The resulting amplitude spectrum has a "hashy" structure with rapid scintillations, which are caused by multipath. When frequency averaging is applied, the rapid variations are removed, generating the smoothed curve of Figure 10(d). The figure corresponds to the average chamber insertion gain for this antenna configuration. The remaining structure in Figure 10(d), after frequency averaging, is due to antenna input mismatch effects. The curve could be further smoothed by applying mismatch corrections. However this was not done, since the effects of antenna mismatch errors were outside the scope of the ITS study.

Of particular interest are several cavity resonance peaks below 10 MHz in Figure 10(c), highlighting the large size and volume of this facility. These cavity resonances are quite visible below the nominal cutoff frequency of 100 MHz for the discones. Figures 11(a)-(d) show a corresponding set of results for a pair of log-periodic antennas. The frequency-averaged insertion gain curve of Figure 11(d) is smoother than the result obtained with the discone antennas shown above. This is due to a better antenna input impedance match with a reduced source/antenna mismatch. The insertion gain curves exhibit a rapid decrease below 300 MHz, which is due to the 290 MHz low-frequency cutoff of the log-periodic antennas. The higher cutoff frequency of the log-periodic antennas suppress the low-frequency cavity modes, and they are not visible in the plots.
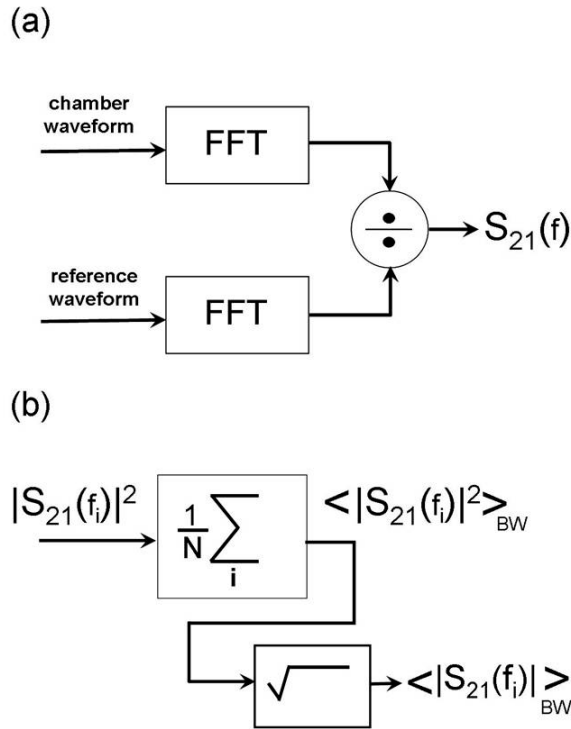
Figure 9. (a) Calculation of S_{21} from the chamber and reference waveforms. (b) The frequency averaging process.
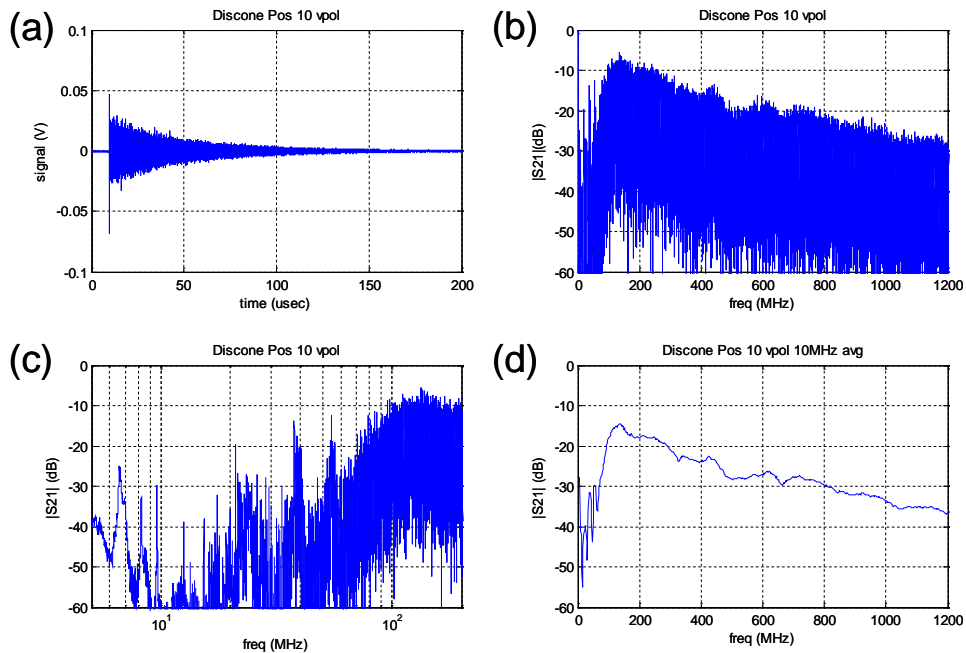
Figure 10. Position 10 waveform and amplitude spectrum obtained with discone antennas. (a) Position 10, vpol waveform. (b) Associated amplitude spectrum. (c) Amplitude spectrum plotted on a log frequency scale (5–200 MHz). (d) Frequency-averaged insertion loss (BW=10 MHz).
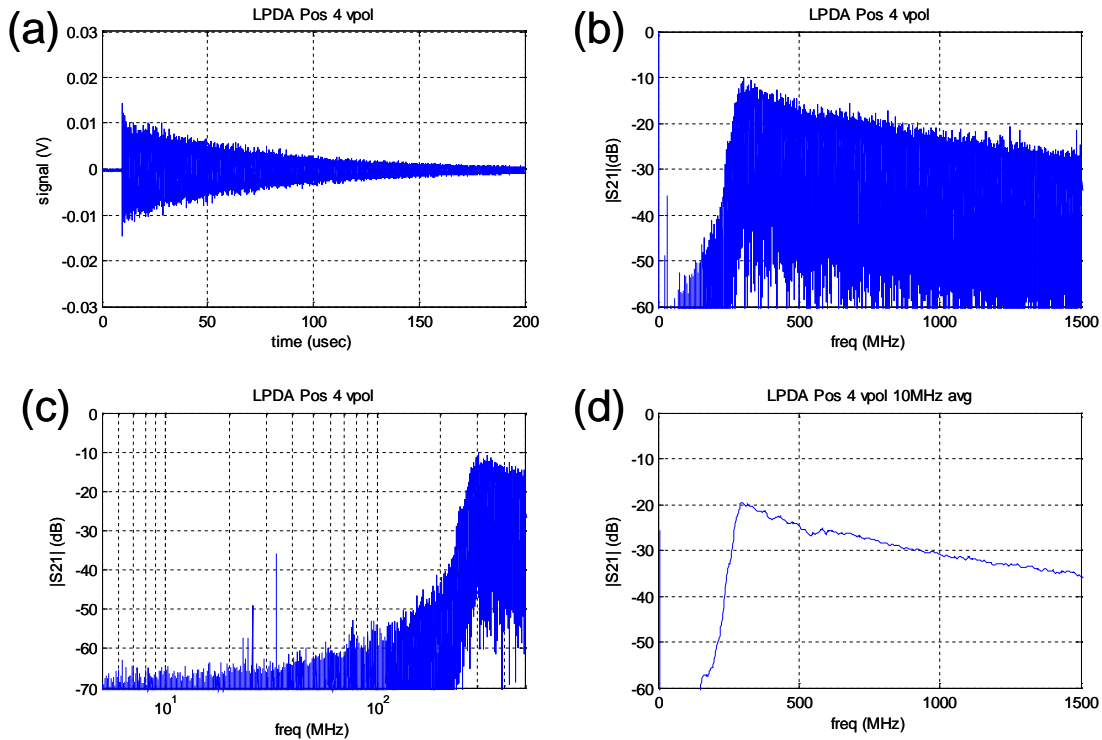
Figure 11. Position 4 oscilloscope waveform and amplitude spectrum obtained with log-periodic antennas. (a) Position 4, vpol waveform. (b) Associated amplitude spectrum. (c) Amplitude spectrum plotted on a log frequency scale (5–500 MHz). (d) Frequency-averaged insertion loss (BW=10 MHz).

If we now plot the averaged results for a number of different antenna configurations, we can better describe the statistical field uniformity of the chamber. Figure 12 shows average insertion gain plots for 20 antenna configurations and three types of antennas. The resulting curves are tightly clustered with a maximum spread of less than 3 dB, indicating good field uniformity over the scan plane.

The same analysis was applied to the vertical scan, and the results are summarized for the three antennas in Figure 13. As was mentioned earlier in section 4, the hard trigger configuration of Figure 2(b) was not used for the vertical scan. Instead, the sweeps were initiated directly from the received signal, using the oscilloscope's internal trigger. Difficulties were encountered with this triggering method, due to wireless signals that occurred intermittently inside the SPF. When a wireless signal was present, it would cause jitter in the received waveforms and "smear out" the averaged waveform. Attempts were made to identify the source of the interference, but with no success. NASA engineers speculated that this might be due to wireless networks within the SPF building. The chamber itself was not EMI hardened, so signals could penetrate into the chamber through gaps in the door, electrical conduits, and the complex vacuum pipe system. The frequency-averaged transmission data are shown in Figure 13, where a scalloping is seen primarily in the discone and LPDA results. This is attributed to the jitter caused by the wireless interference. The values are similar to those obtained in Figure 12.
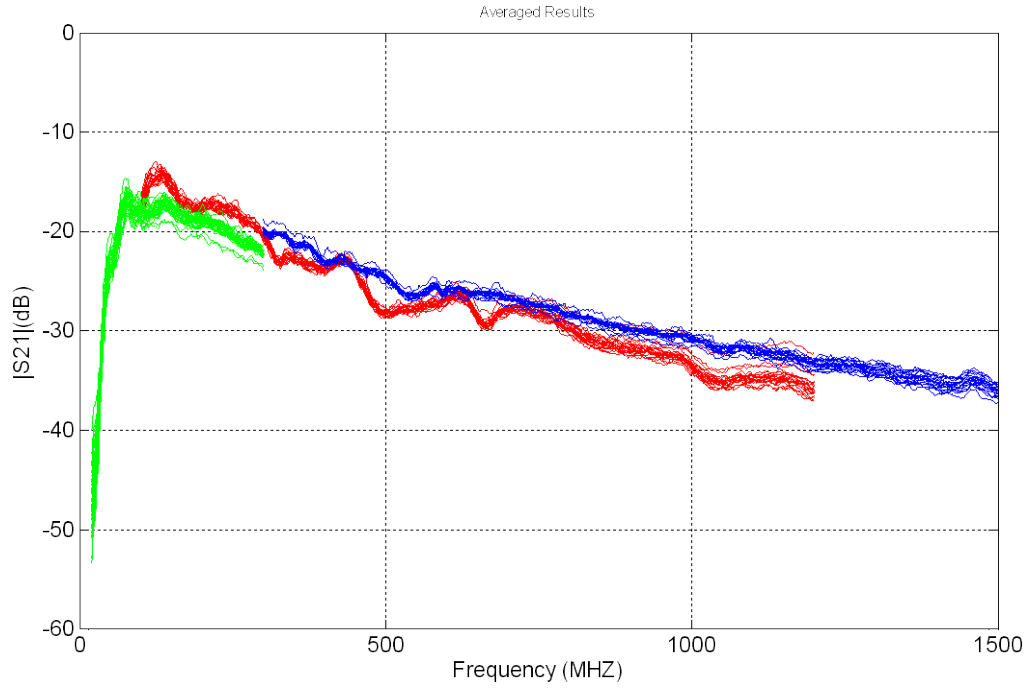
Figure 12. Frequency-averaged (BW=10 MHz) results obtained over all of the horizontal scans for the three antenna types (20 positions): green (biconical), red (discone), and blue (log-periodic).
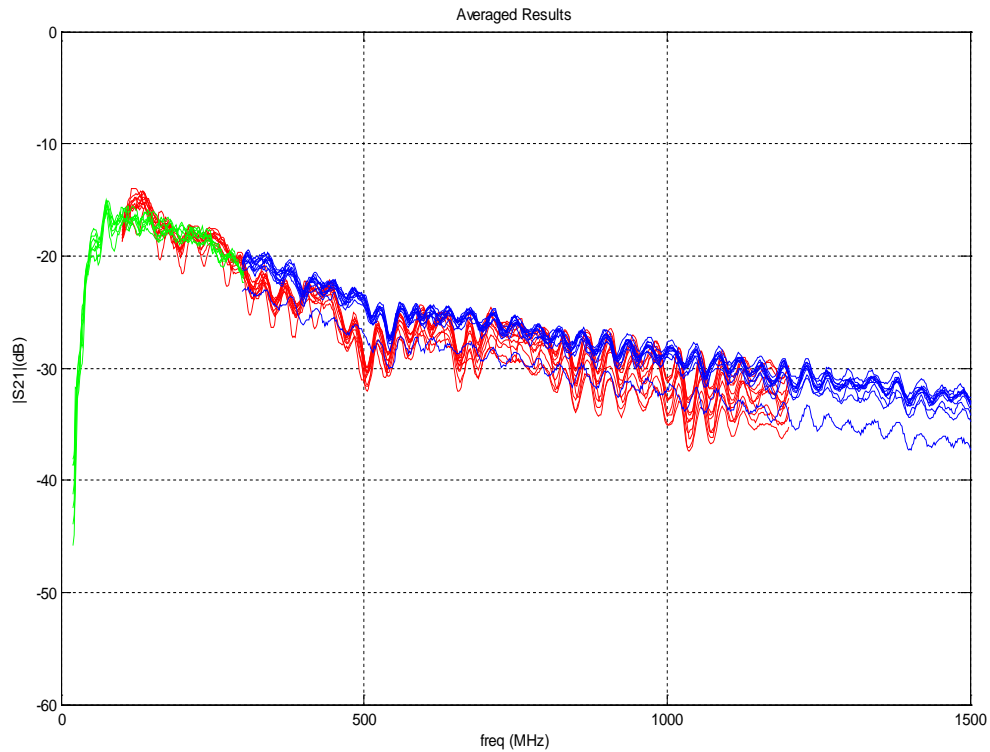
Figure 13. Frequency-averaged (BW=10 MHz) results obtained over all of the vertical scans (14 positions) for the three antenna types: green (biconical), red (discone), and blue (log-periodic).

13

7 EARLY-TIME FOCUSING

One of the questions that NASA had at the onset of this effort was whether or not the spherical dome of the SPF exhibits focusing effects or caustics. One reason for carrying out a vertical scan was to see if any focusing effects did, in fact, occur. The dome of the SPF has a radius of curvature of 50'(15.2 m) if we assume it has a spherical shape. From geometric optics of spherical reflectors, we should see a focus at one half of the radius of curvature of the dome, or approximately 25' (7.6 m) below the top of the dome (97' (29.6 m) above the floor).

Figure 14 shows two scope waveforms that were obtained in the vertical scan for biconical transmitting and receiving antennas with the transmitting antenna oriented for vertical polarization and the receiving antenna horizontally polarized. In order to see this effect, we need to look at the initial wave front arrival which contains the high-frequency geometric-optics field [5], [6]. Figure 14(a) shows the waveform obtained with the transmitter set at a height of 90'. In Figure 14(b) the corresponding waveform at the 100' height is shown, and a large spike occurs approximately 50 ns after the wave front arrival. We believe this is due to focusing. This is a wideband, early-time effect and comprises only a small fraction of the total waveform energy. The impact of this effect will depend on the actual E3 testing scenario.

The waveform is plotted over a 0.5 μsec interval, and it shows the early-time response of the chamber. The time scales represent a relative, not absolute time since the oscilloscope was operated in a free-trigger sweep mode, and the trigger delays were adjusted for display purposes, which accounts for the time offset between the waveforms and the scale readings.

Figure 14. Biconical antenna early-time, time-domain signals obtained on the vertical scan. (a) Transmitting antenna at a 90' (27.4 m) height. (b) Transmitting antenna at a 100' (30.5 m) height with the focusing effect annotated in red.

8 POWER-DECAY CHARACTERISTICS

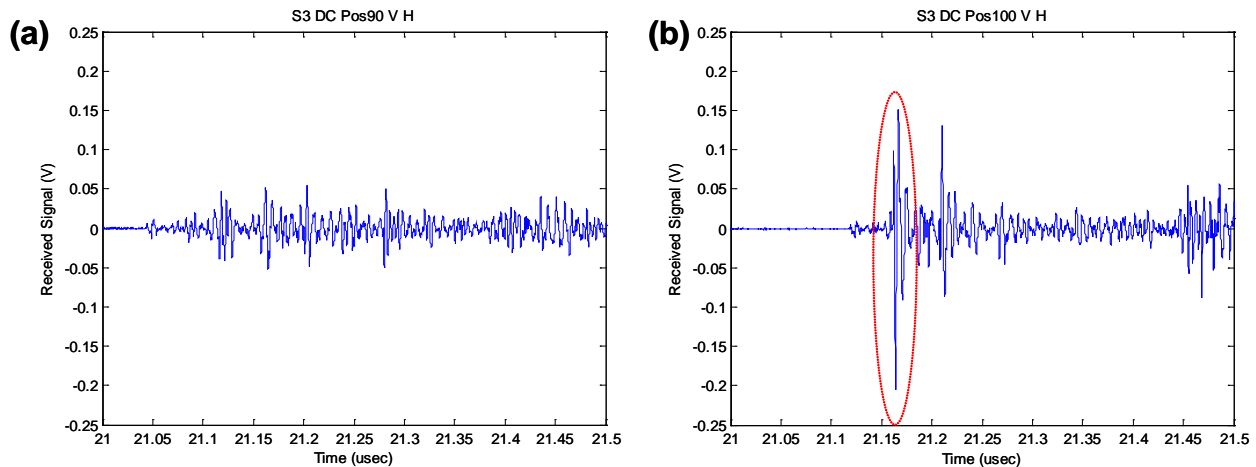The analysis of the chamber time-decay characteristics is implemented using a combination of joint time-frequency analysis (JTFA) [7], [8] and frequency averaging. This process is shown in Figure 15. The joint-time frequency analysis is implemented by applying a windowed FFT to the measured chamber waveform, denoted by *ch(t)*. A sliding window approach is used . This is implemented by subdividing the time-domain record into short blocks and then applying an FFT to each. A Blackman taper is used with window widths that range from 1–10 μsec. The choice of window width is dictated by a combination of desired frequency resolution and signal-to-noise ratio. For the results shown here, we used a 10 μsec wide window and performed FFT's at successive 5 μsec increments. This process generates a sequence of spectrum amplitude vectors that are a function of both the window position τ and frequency f_n, which results in a two-dimensional array. By selecting a particular FFT output bin (or a group of adjacent bins), we compute amplitude spectra for successively larger window positions and infer chamber decay rates as a function of frequency. Thus, we can examine amplitude spectrum decay rates over selected frequency bands.

Figure 16(a) shows the output of a 300 MHz FFT bin for a 10-μsec wide Blackman window plotted at 5-μsec intervals. The resulting signal decays with irregular variations, which are caused by interference between closely-spaced chamber cavity modes. These fluctuations make it difficult to estimate the rate of decay. However, if we frequency average the FFT bin outputs over a span of 10 MHz, we obtain the smoothed and much-improved result of Figure 16(b). We now apply a least-squares (LS) fit to the power-averaged result to obtain a linear estimate of the power decay rate, shown by the red line in Fig. 16(b). The slope of this line is used to estimate the time it takes the power to decay to 36% ($1/e$) of its original level. In decibels, this corresponds to a change of -4.3 dB. The range over which the LS fit is performed is 40–160 μsec in order to ensure that we are on the decaying portion of the signal and well above the system noise limit. It is noted that the power decay rate is twice that of the electric and magnetic field decay rates.
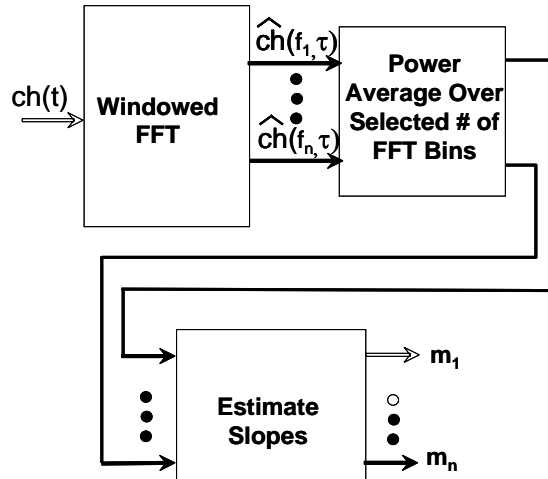

Figure 15. Block diagram of the joint time-frequency analysis used to determine power decay rates.
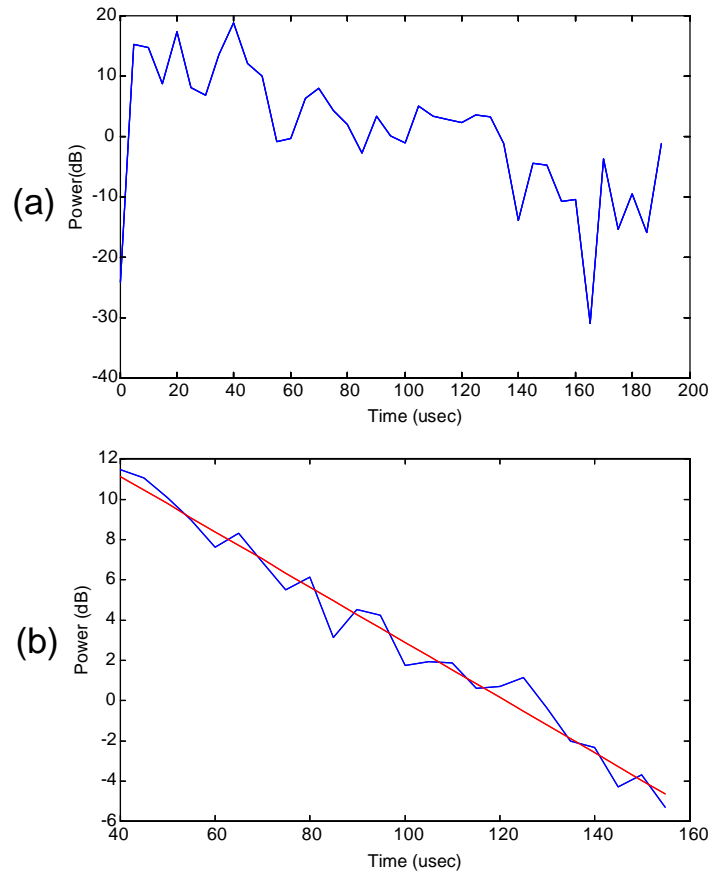
Figure 16. (a) Windowed FFT output at a single FFT output bin (300 MHz) plotted at 5 ns intervals. (b) Frequency-averaged (BW=10MHz) output (blue) and corresponding slope estimate (red) obtained at position 1 (log-periodic antennas).

Some selected JTFA results are shown in Figures 17 and 18, in which we plot both the frequency averaged and resulting LMS slope estimates. Figure 17 shows a set of nine graphs, plotted at 5 MHz intervals, in the frequency range of 65–105 MHz. Figure 19 shows a corresponding set plotted over the range of 785–825 MHz. In both cases, the averaging bandwidth was 10 MHz (±5 MHz about each selected frequency). The LMS linear slope predictions are plotted in red, and the frequency averaged data are plotted in blue. If one compares the two sets of plots, the resulting slopes of the lower frequency set are noticeably steeper. This indicates higher losses at the lower frequencies. This also highlights the frequency variability of the chamber losses and the power of JTFA analysis.

For each antenna configuration, the power decay rate was computed at 5 MHz intervals. Figure 19 shows results for all antennas and polarizations for the entire horizontal scan. The results are tightly clustered, with spreads that increase with frequency. Below 500 MHz, observed variations are typically less than 5 µsec. Above 500 MHz, maximum spreads of approximately 10 µsec occur. The results for the three antenna types overlap and align quite nicely. This is due to a highly reverberant environment that effectively "washes out" the antenna directivity (over their operational ranges) [3]. The decay rates also exhibit good uniformity throughout the scans, analogous to those of the insertion loss.

Figure 17. Frequency-averaged power decay (BW=10 MHz; blue) and LMS estimates (red) plotted in 5 MHz increments in the frequency range of 65–105 MHz.
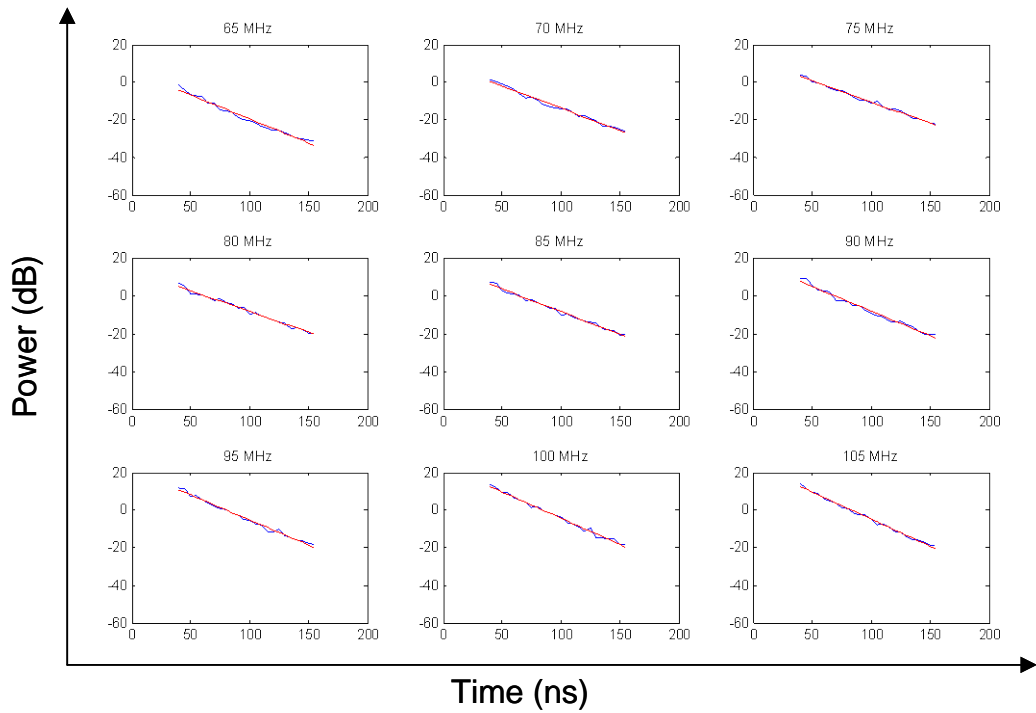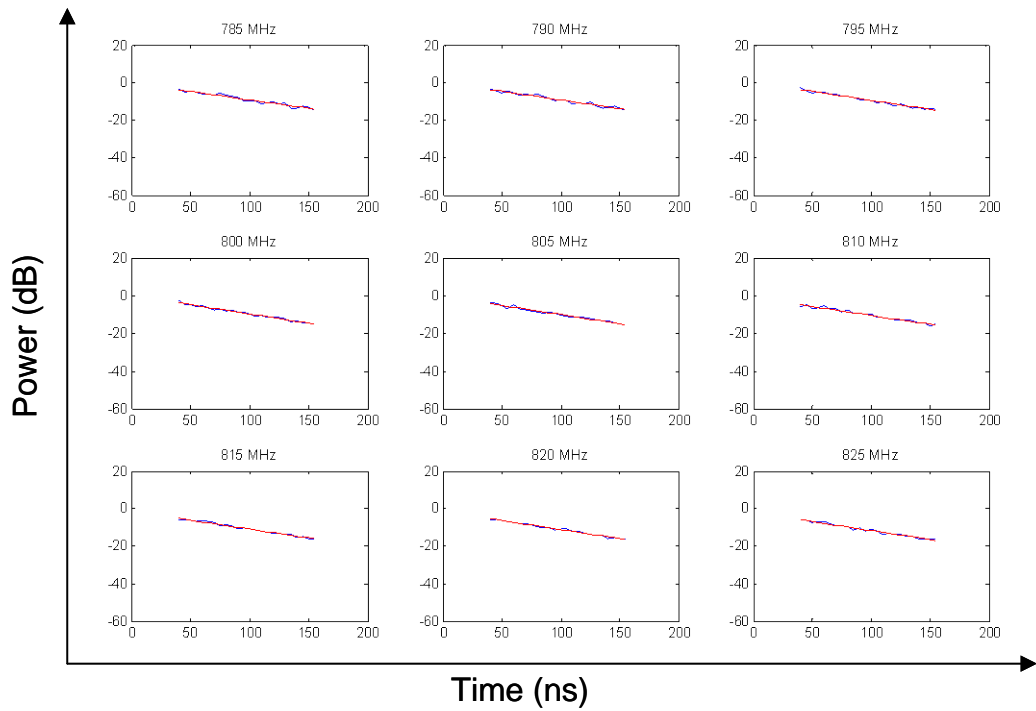

Figure 18. Frequency-averaged power decay (BW=10 MHz; blue) and LMS estimates (red) plotted in 5 MHz increments in the frequency range of 785–825 MHz.
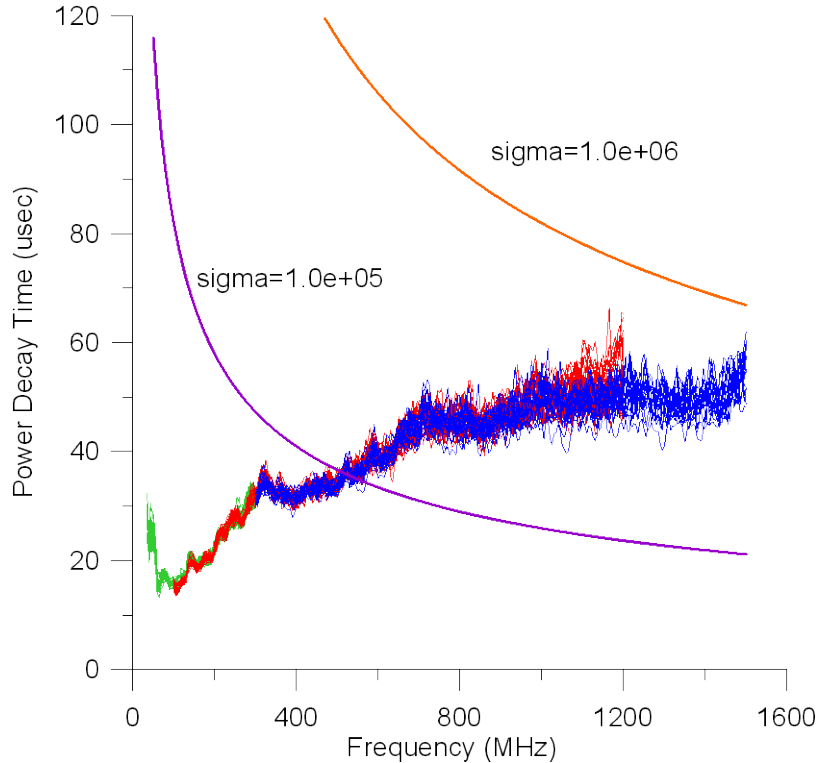
Figure 19. Power-decay time results obtained over all of the horizontal scans for three antenna types (20 positions): green (biconical), red (discone), and blue (log-periodic). Decay time calculations (from [3]) are provided, based on skin-effect losses only for assumed wall conductivities of $\sigma = 10^5$ (purple), $\sigma = 10^6$ (orange).

The decay times exhibit some rather interesting functional behavior. Below frequencies of 100 MHz, the decay times decrease rapidly, reaching minimum values in the neighborhood of 13 to 18 μsec. As the frequency is increased above 100 MHz, the decay times increase steadily up to about 300 MHz. With the exceptions of several minor dips, the decay rates continue to increase up to the highest measured frequency of 1500 MHz.

The 30–300 MHz range is dominated by the antenna loading effects, which is typical for large complex cavities [3]. Above 300 MHz, the trend is more complex. Clearly, if wall losses were the dominant effect, we would expect to see the decay time decrease with inverse square root of the operating frequency. This might be anticipated at higher frequencies, where the antenna loading is far less significant. Instead, the decay times continue to increase (at a diminishing rate) with frequency, which cannot be explained by wall losses alone.

It appears that there are additional loss mechanisms. The flattening of the decay rates above 700 MHz might be due to a combination of aperture leakage and lossy objects. At the time these tests were conducted, the SPF chamber was not EMI hardened and wireless signals were observed leaking into the closed chamber during some of the measurement sequences, which supports the hypothesis of aperture loading in the SPF. Also, the doors are sealed with a rubber material that could provide additional RF volumetric losses. Clearly, more analysis and further investigation are needed to better understand the power-decay characteristics.
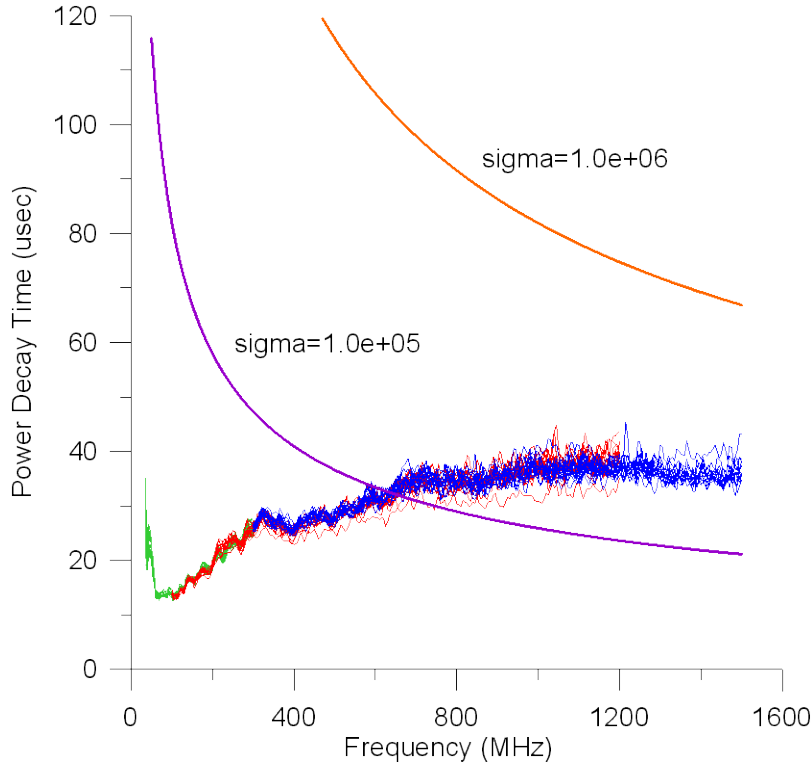
Figure 20. Power-decay time results obtained over all of the vertical scans for three antenna types (14 positions): green (biconical), red (discone), and blue (log-periodic). Decay time calculations (from [3]) are provided, based on skin-effect losses only for assumed wall conductivities of $\sigma = 10^5$ (purple), $\sigma = 10^6$ (orange).

Figure 20 shows the corresponding decay results for the vertical scan. All of the measurements using the three sets of antennas are included. The resulting decay characteristics show similar functional behavior to the horizontal scans. Above 500 MHz, the vertical scan results have somewhat lower decay rates and tighter clustering, which is likely due to volumetric loading of the human operator inside the chamber for this series of tests. The wireless interference jitter described previously had little impact on the power decay results.

9   ITS/NIST INSERTION GAIN COMPARISONS

A team of engineers from the National Institute of Standards and Technology (NIST) performed a separate series of transmission measurements inside the SPF six months after the completion of the ITS effort. They measured transmission gain using a vector network analyzer/optical link combination, which directly measures the magnitude and phase of S_{21}. NIST used a similar measurement scanning methodology to that previously developed by ITS engineers. In addition, NIST engineers applied antenna mismatch corrections to obtain refined estimates of insertion gain.

While the ITS time-domain system can be used to compute S_{21}, it is more precise to use the measured power-decay times to infer insertion gain. Hill [3] provides equations that permit the calculation of insertion gain from the measured power-decay times. There are several reasons for using this approach. First, when we acquired the waveforms, we limited the time window of the received waveform to 200 μsec, during which, the signal decays to approximately 5% of its original amplitude. This results in a truncation error in $|S_{21}|$ of approximately ±0.5 dB. This choice was made because longer waveform records would have significantly increased data acquisition time. An additional error is caused by amplitude drift in the pulse generator. This varied as much as 1 dB during the course of a full-day measurement. Also, no mismatch corrections were applied to the insertion data, which contributes additional measurement uncertainties. That said, even with these systematic errors, the insertion loss results presented here indicate good chamber statistical field uniformity.

The ITS system and associated signal processing, however, provide precise estimates of power decay time. First, the computation is based on a single waveform, so it is not subject to either amplitude drift or truncation effects.

From Hill [3], we have

$$Q = \frac{16\pi^2 V}{\eta_t \eta_r \lambda^3} \, |S_{21\_avg}|^2,$$ (1)

where Q is the chamber quality factor, V is the chamber volume (m³), λ is the RF source wavelength (m), $|S_{21\_avg}|$ is the frequency-averaged insertion gain, and η_t and η_r are the transmitting and receiving antenna efficiencies respectively.

Also, the power decay time and the chamber quality factor are related by

$$Q = 2\pi f \tau,$$ (2)

where f is the RF source frequency in Hz and τ is the power-decay time in seconds. Combining (1) and (2) and substituting wavelength for frequency obtains:

$$|S_{21\_avg}|^2 = \frac{c\lambda^2}{8\pi V} \eta_t \eta_r \tau$$ (3)

20

where $c = 3.0 \times 10^8$ m/sec and τ is the measured power decay time (sec). Equation (3) can now be used to calculate insertion gain from the measured power decay times. We used a two-step process to compare our results with those of NIST. We took all of the horizontal scan power-decay data and averaged the decay times over all of the positions and polarizations. This was done for the three antenna types. The result of this process is a frequency-dependent decay time. These results were then applied to (3) to obtain insertion gain. Since the transmitting and receiving antenna efficiencies have not been characterized for the antennas used, we assume the antennas are lossless with $\eta_t = \eta_r = 1$. This assumption provides an upper limit on the insertion gain.

Figure 21 shows the ITS/NIST insertion gain intercomparisons. The ITS data are plotted for the three antenna types. The results for the different antenna types are closely aligned in the overlapping frequency ranges, which indicate that mismatch losses have a minimal impact on the measured decay times. The NIST VNA data that are shown are derived from a combination of antenna types with antenna mismatch corrections applied. The ITS results are offset by 1–2.5 dB from those of NIST. The data sets agree fairly well, and the trends are very similar, lending confidence to both sets of measurements. Closer agreement might be obtained with additional antenna efficiency corrections applied to the ITS data. In a recent paper, Krauthäuser [9] performed a series of antenna efficiency measurements in several reverberation chambers using narrowband, pulsed, time-decay measurements. He found that the antenna efficiencies for a set of LPDA antennas varied over the range $0.6 \leq \eta \leq 0.75$ in the frequency range of 100–1000 MHz. The 2.5 dB difference observed above 300 MHz in Figure 21 could be almost eliminated if we assume $\eta_t = \eta_r = 0.75$. Clearly, more measurements and research are needed to better understand the differences in the data sets and to obtain improved correlation.

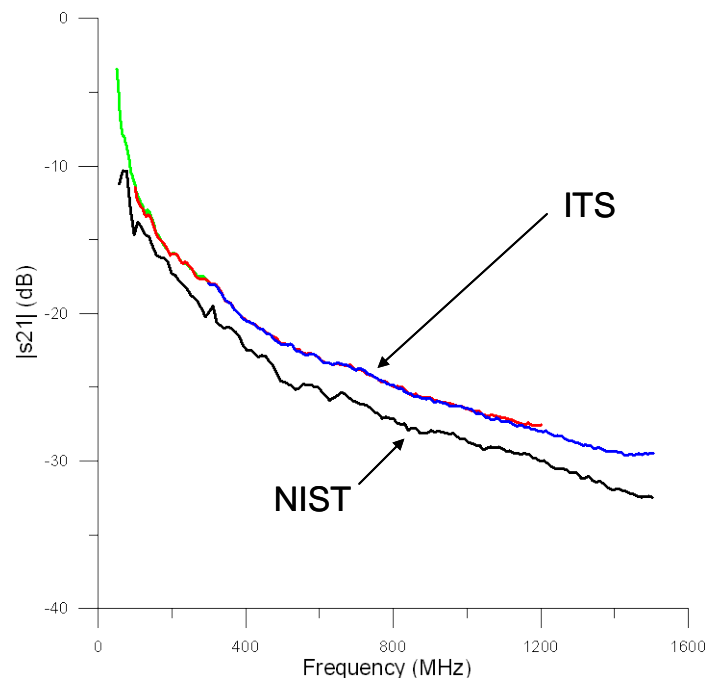Figure 21. ITS chamber insertion gains inferred from measured decay times (bicones-green, discone-red, lpda-blue) with the assumption $\eta_t = \eta_r = 1$. The combined NIST VNA results are shown in the black curve (courtesy of John Ladbury of NIST).
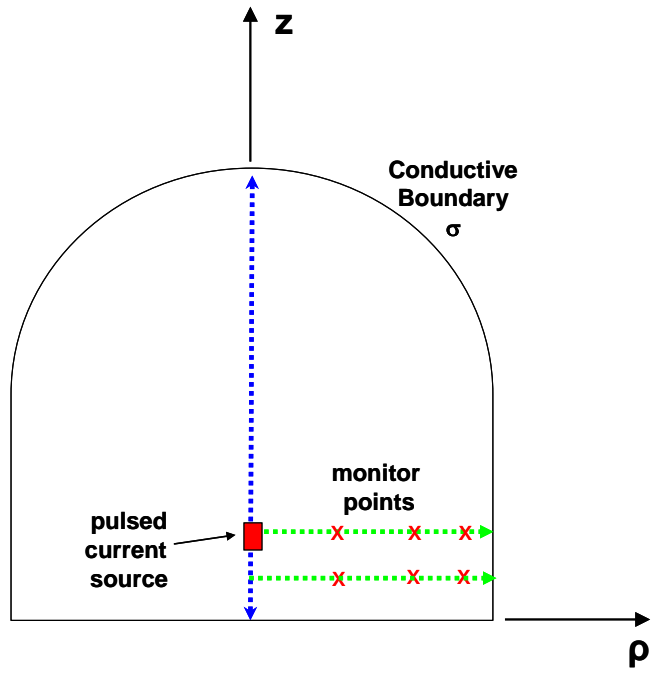
Figure 22. Two-dimensional, axially-symmetric FDTD model of the SPF, showing the pulsed current source and monitor point locations (marked with x's).

10 AXIALLY-SYMMETRIC FINITE-DIFFERENCE TIME-DOMAIN MODEL

A two-dimensional FDTD model has been developed for the SPF based on axial symmetry. A two-dimensional approximation can be made with the following assumptions: 1) we assume that the chamber is axially symmetric about the vertical center axis of the chamber, and 2) we restrict the source current to be on this axis. With these restrictions, Maxwell's equations can be formulated in cylindrical coordinates with two possible sets of transverse field components with respect to the z axis: transverse magnetic TM_z (E_ρ, H_ϕ, E_z) for an electric current source, or transverse electric TE_z (H_ρ, E_ϕ, H_z) for a magnetic current source. The ITS model employs a z-directed electric current source located on the chamber axis as is shown in Figure 22. The current source is the simple derivative of a Gaussian waveform of unit amplitude shown in Figure 23(a). The pulse has significant energy for approximately 5 ns with a resulting amplitude spectrum extending beyond 1 GHz shown in Figure 23(b). The Yee cells are spaced at 3.048 cm, with a resulting lattice bandwidth of approximately 1 GHz. The wall losses are incorporated into the model using a full-wave formulation described in Kunz and Luebbers [10] . Simulations were performed for a number of different source/monitor point combinations with wall conductivities of 10^5 and 10^6 S/m. The source and monitor point locations correspond to some of the horizontal scan measurement locations

Figure 24(a) shows a computed electric field time-domain waveform with an assumed wall conductivity of $\sigma = 10^5$ with a monitor point location of $\rho = 46'$(14.0 m) and z = 22' (6.7m) and a source location of $\rho=0'$ and z=20' (6.1 m). The resulting time-domain waveform exhibits a single exponential decay envelope and is similar to the waveforms obtained at other source/monitor point locations.
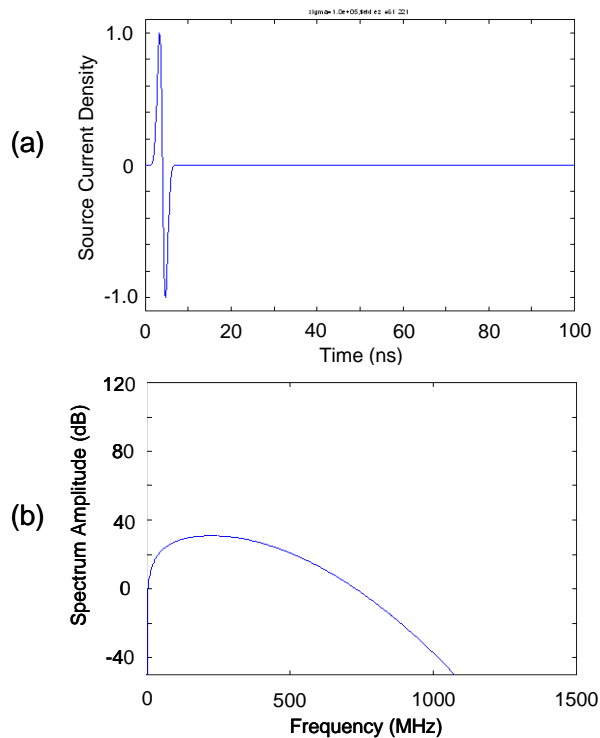

Figure 23. (a) FDTD current pulse. (b) Current density amplitude spectrum.
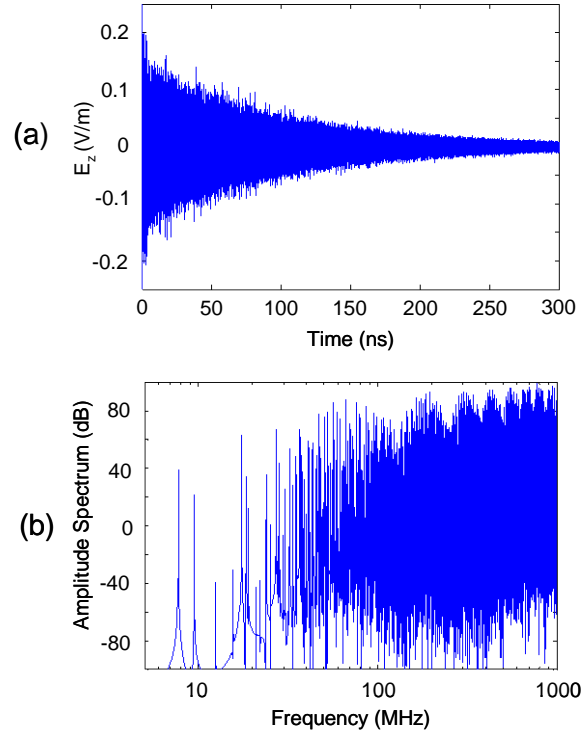
23

Figure 24. (a) Z-component of the electric field computed at ρ=46'(14.0 m), z = 22' (6.7 m) with a current source located at ρ=0', z = 22' and σ = 10^5 (S/m). (b) Normalized amplitude spectrum.

In order to view the FD-TD results in the frequency domain, we take the ratio of the spectrum amplitudes of the computed electric-field component and the current source:

$$SA_{normalized} = \frac{|FFT(E(t))|}{|FFT(I(t))|},$$ (4)

where $SA_{normalized}$ is the normalized amplitude spectrum, $E(t)$ is the computed electric-field component, $I(t)$ is the source current component, and FFT denotes the fast Fourier transform. Applying the waveforms of Figures 24(a) and 23(a) to (4) yields the normalized spectrum of Figure 24(b). At frequencies below 25 MHz, we see isolated cavity modes, but above that, the modes become more closely spaced due to increasing modal density. Strong modes are predicted below 10 MHz—a result that is consistent with the measurements. Figure 25 shows the corresponding early-time waveform. The direct arrival is seen at approximately 22 ns, followed by an increasing number of chamber reflections. The rate of arrival of chamber reflections increases steadily with time and is indistinguishable beyond 300 ns.

Figure 26 shows 200 μsec long time-domain records of E_z at the six monitor points shown in Figure 22. The amplitude does show some decrease as the radius increases, but there is not much variation at the two heights. This trend was not seen in the measurements, which might be due to the perfect symmetry and lack of diffusers (e.g. door buttresses) in this model. The computed waveforms are similar in character, and all of them have a distinctive single-exponential decay envelope. There is also a strong resemblance with respect to shape and rates of decay to the

measured full-bandwidth waveforms. Figure 27 shows the electric fields for a wall conductivity of $\sigma=10^6$ S/m. Similar trends are seen with respect to the radial and height dependence of the waveform amplitudes. Once again, the waveforms have a single-exponential decay envelope. The decay rate is several times longer in this case due to the higher wall conductivity.

A JTFA analysis was performed on all of the computed fields and the results are summarized in Figure 28 along with theoretical predictions using formulas in [4]. The analysis parameters (e.g. window width and taper) which are used here are identical to the ones used previously on the measured data in section 8. Both the FD-TD theoretical predictions assume wall losses due to skin effect. The results track well at all six positions for both conductivities, indicating that the FD-TD model is accurate. In addition, the results validate the JTFA analysis software and parameter selection. Since we have not incorporated other loss types (e.g. antenna, aperture, volumetric), the JTFA analysis exhibits a functional behavior that is quite different from that of the measurements. Additional losses will need to be incorporated into the FD-TD model to replicate the measured power-decay characteristics.
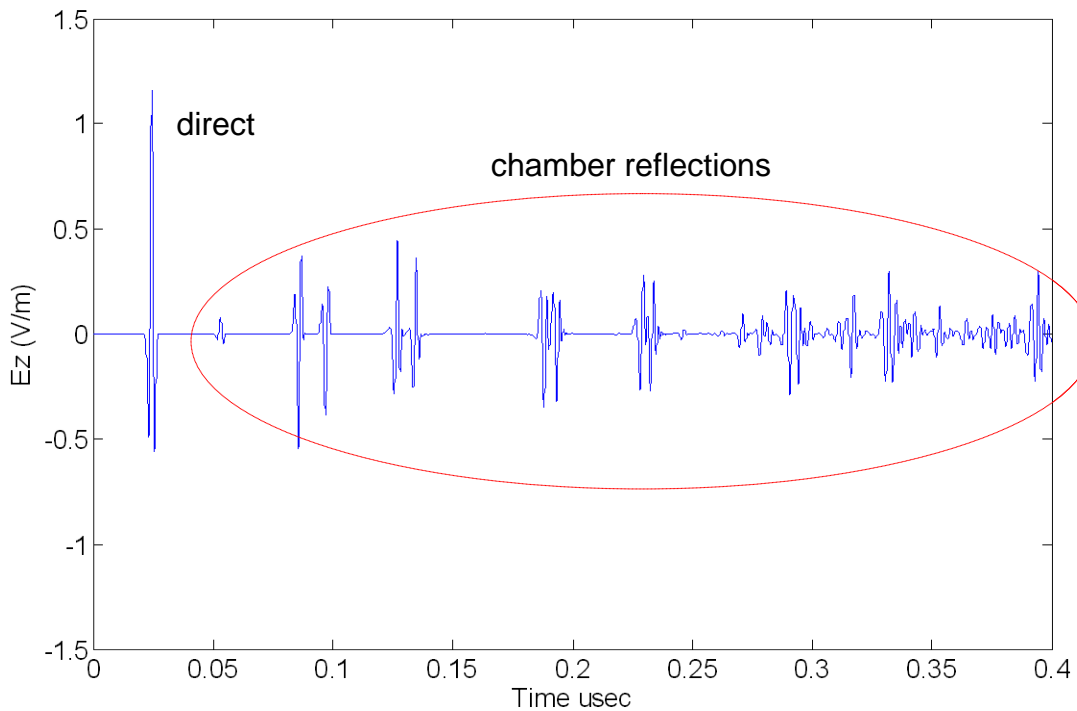

Figure 25. Early-time time waveform for E_z at ρ=22', z = 20' showing both the direct component and subsequent chamber reflections.
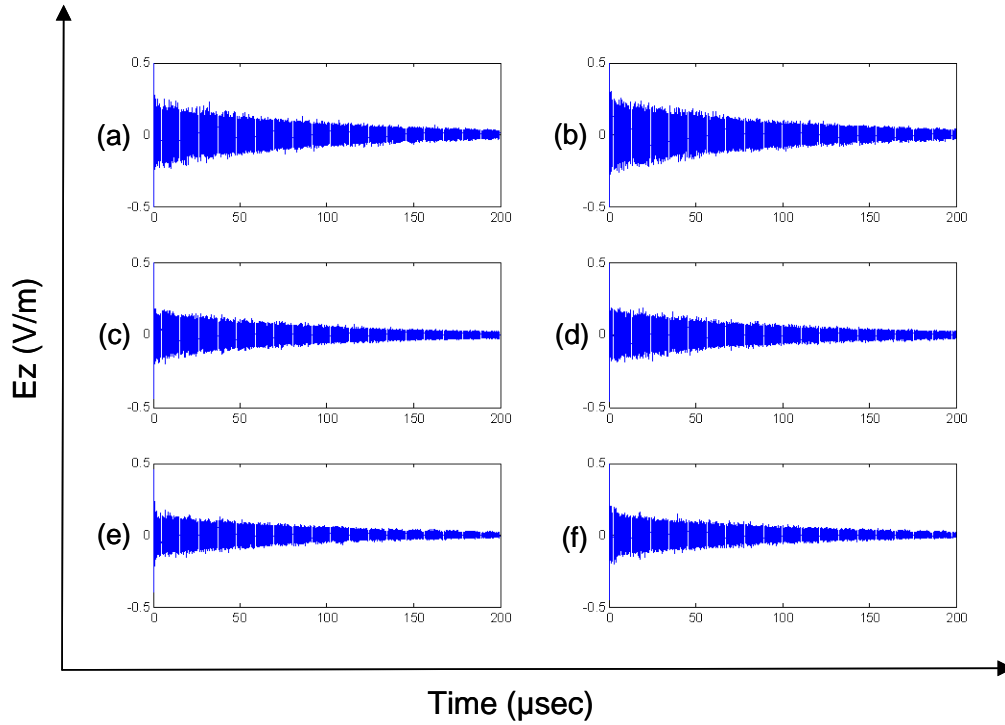
Figure 26. Ez waveforms obtained at six monitor point locations with a wall conductivity σ=105 S/m and a source location ρ=0', z =20'. (a) ρ=20', z =22'. (b) ρ=20', z =10'. (c) ρ=36', z =22'. (d) ρ=36', z =10'. (e) ρ=46', z =22'. (f) ρ=46', z =10'.
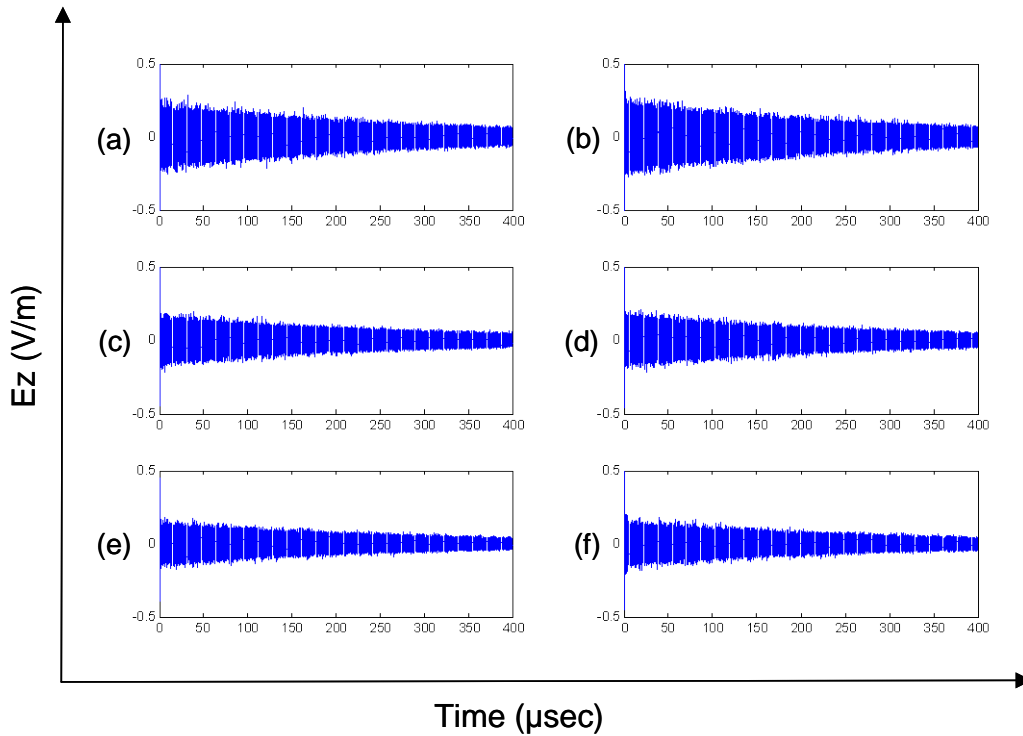
Figure 27. E_z waveforms obtained at six monitor point locations with a wall conductivity $\sigma=10^6$ S/m and a source location ρ=0', z =20'. (a) ρ=20', z =22'. (b) ρ=20', z =10'. (c) ρ=36', z =22'. (d) ρ=36', z =10'. (e) ρ=46', z =22'. (f) ρ=46', z =10'.

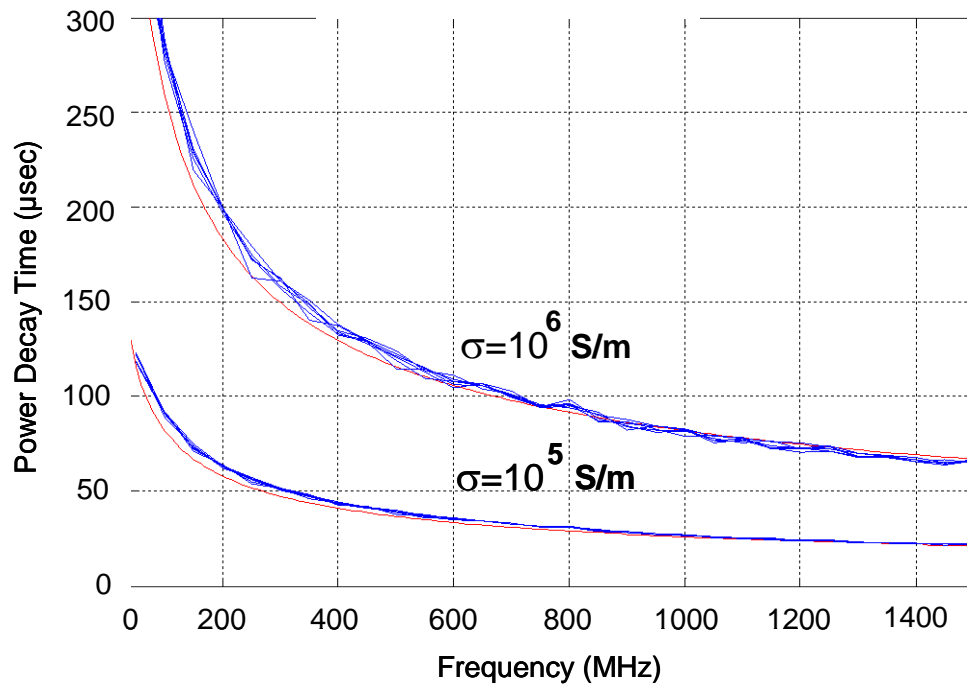Figure 28. JTFA analysis results (blue) for Ez at all of the source/monitor point configurations and two conductivities. Theoretical predictions based on wall skin-effect losses are plotted in red.

11 CONCLUSIONS

This effort highlights the power and utility of direct-pulse time measurements and joint time-frequency analysis. The measurement system performed well and with high efficiency. The results obtained were both repeatable and accurate.

The measurement effort provided much insight into the electromagnetic environment of the NASA SPF chamber. The biggest surprise was the robust diffusion and depolarization that was observed, given that there was no paddle present. One possible source are the two large door buttresses, which could provide a strong depolarization effect; more research is needed here. Another finding was the complex loss mechanisms which are due to a combination of antenna loading, conductive wall losses, and possible losses due to aperture/volumetric loading. The results indicate that the SPF chamber has the potential to operate as a reverberation chamber over a wide frequency range. Further measurements and numerical electromagnetic simulations will be required to determine the operational frequency range and the achievable level of performance.

12 ACKNOWLEDGEMENTS

13 REFERENCES

[1] R.T. Johnk, J.D. Ewan, P. M. McKenna, R. L. Carey, N. DeMinco, and K.A. Shalkhauser, "Time-domain pulsed measurements of the NASA space power facility," *IEEE International Symposium on EMC*, 18 to 21 August 2009, pp. 187 to 192.

[2] J.M. Ladbury, R.T. Johnk, and A.R. Ondrejka, "Rapid evaluation of mode-stirred chambers using impulsive waveforms," NIST Technical Note 1381, 1996.

[3] D. A. Hill, "Electronic mode stirring for reverberation chambers," *IEEE Trans. Electromagn. Compat.*, vol. 36, pp. 294–299, 1994.

[4] D. A. Hill, *Electromagnetic Fields in Cavities: Deterministic and Statistical Theories,* New York: IEEE Press, 2009.

[5] M. Kline and I. W. Kay, *Electromagnetic Theory and Geometrical Optics*, New York: John Wiley & Sons, 1962.

[6] L. B. Felsen, "Progressing and oscillatory waves for hybrid synthesis of source excited propagation and diffraction, *IEEE Trans. Antennas Propagat.*, vol. AP-32, pp. 775–796, 1984.

[7] L. Cohen, *Joint Time-Frequency Analysis: Theory and Applications,* New York, NY, Prentice-Hall, 1995.

[8] R.T. Johnk, B. Archambeault, and D. Novotny, "Using joint time-frequency analysis to enhance time-domain numerical EMC simulations," *Interference Technology, Annual Guide*, 2003.

[9] H.G. Krauthäuser and M. Herbrig, "Yet another efficiency measurement method in reverb chambers," *IEEE International Symposium on EMC*, 25 to 30 July 2010, pp. 536 to 540.

[10] K. S. Kunz and R. J. Luebbers, *The Finite Difference Time Domain Method for Electromagnetics*, Boca Raton, Fl: CRC Press, 1993.

FORM **NTIA-29** U.S. DEPARTMENT OF COMMERCE
(4-80) NAT'L. TELECOMMUNICATIONS AND INFORMATION ADMINISTRATION

BIBLIOGRAPHIC DATA SHEET

1. PUBLICATION NO. TR-10-471	2. Government Accession No.	3. Recipient's Accession No.
4. TITLE AND SUBTITLE Time-Domain Propagation Measurements of the NASA Space -Power Facility		5. Publication Date September 2010
		6. Performing Organization Code
7. AUTHOR(S) R. T. Johnk, J. D. Ewan, P. M. McKenna, R. L. Carey, N. DeMinco		9. Project/Task/Work Unit No. 3108011-300
8. PERFORMING ORGANIZATION NAME AND ADDRESS Institute for Telecommunication Sciences National Telecommunications & Information Administration U.S. Department of Commerce 325 Broadway Boulder, CO 80305		
		10. Contract/Grant No.
11. Sponsoring Organization Name and Address National Telecommunications & Information Administration Herbert C. Hoover Building 14th & Constitution Ave., NW Washington, DC 20230		12. Type of Report and Period Covered
14. SUPPLEMENTARY NOTES		

15. ABSTRACT (A 200-word or less factual summary of most significant information. If document includes a significant bibliography or literature survey, mention it here.)

This report describes a recent measurement effort conducted by the Institute for Telecommunication Sciences at a chamber located at the NASA Space Power Facility (SPF) in Sandusky, Ohio. The paper describes the chamber and the measurement system, and provides some selected time- and frequency-domain results. A detailed description of the measurement procedures and post-processing is provided. The results obtained indicate that the SPF chamber exhibits robust reverberant behavior. The flexibility and efficiency of time-domain measurements is also demonstrated.

16. Key Words (Alphabetical order, separated by semicolons)

antenna; biconical; chamber; decay time; direct pulse; discone; electromagnetic; finite-difference time-domain; fast Fourier transform; impulse; joint time-frequency analysis; log-periodic; oscilloscope; reverberation; ultra wideband.

17. AVAILABILITY STATEMENT ☒ UNLIMITED.	18. Security Class. (This report) Unclassified	20. Number of pages 44
	19. Security Class. (This page) Unclassified	21. Price:

NTIA FORMAL PUBLICATION SERIES

NTIA MONOGRAPH (MG)
A scholarly, professionally oriented publication dealing with state-of-the-art research or an authoritative treatment of a broad area. Expected to have long-lasting value.

NTIA SPECIAL PUBLICATION (SP)
Conference proceedings, bibliographies, selected speeches, course and instructional materials, directories, and major studies mandated by Congress.

NTIA REPORT (TR)
Important contributions to existing knowledge of less breadth than a monograph, such as results of completed projects and major activities. Subsets of this series include:

NTIA RESTRICTED REPORT (RR)
Contributions that are limited in distribution because of national security classification or Departmental constraints.

NTIA CONTRACTOR REPORT (CR)
Information generated under an NTIA contract or grant, written by the contractor, and considered an important contribution to existing knowledge.

JOINT NTIA/OTHER-AGENCY REPORT (JR)
This report receives both local NTIA and other agency review. Both agencies' logos and report series numbering appear on the cover.

NTIA SOFTWARE & DATA PRODUCTS (SD)
Software such as programs, test data, and sound/video files. This series can be used to transfer technology to U.S. industry.

NTIA HANDBOOK (HB)
Information pertaining to technical procedures, reference and data guides, and formal user's manuals that are expected to be pertinent for a long time.

NTIA TECHNICAL MEMORANDUM (TM)
Technical information typically of less breadth than an NTIA Report. The series includes data, preliminary project results, and information for a specific, limited audience.

For information about NTIA publications, contact the NTIA/ITS Technical Publications Office at 325 Broadway, Boulder, CO, 80305 Tel. (303) 497-3572 or e-mail info@its.bldrdoc.gov.

This report is for sale by the National Technical Information Service, 5285 Port Royal Road, Springfield, VA 22161,Tel. (800) 553-6847.